First-principles-based phase diagram of the cubic BNC ternary system

Koretaka Yuge,[1] Atsuto Seko,[2] Yukinori Koyama,[3] Fumiyasu Oba,[1] and Isao Tanaka[1,4]

[1]*Department of Materials Science and Engineering, Kyoto University, Sakyo, Kyoto 606-8501, Japan*
[2]*Pioneering Research Unit for Next Generation, Kyoto University, Kyoto 615-8530, Japan*
[3]*Innovative Collaboration Center, Kyoto University, Sakyo, Kyoto 606-8501, Japan*
[4]*Nanostructure Research Laboratory, Japan Fine Ceramics Center, Atsuta, Nagoya, 456-8587 Japan*

The phase diagram for the cubic BNC ternary system in a heterodiamond structure was examined by Monte Carlo simulations and the cluster expansion technique based on first-principles calculations. All the atomic arrangements exhibit positive formation energies, indicating phase separation into cubic BN (c-BN) and diamond. These arrangements show a strong preference for B-N and C-C bonds and disfavor B-C, C-N, B-B, and N-N bonds along the first nearest neighbor coordination. This can be naturally attributed to the oversaturation and undersaturation of the number of electrons for respective first nearest neighbor bonds. First-principles-based lattice-dynamics calculations reveal that the formation of a solid solution between c-BN and diamond decreases vibrational free energy, resulting in a significant enhancement of the solubility for both c-BN and diamond-rich phases. Complete miscibility is achieved over $T=4500$ K, which is higher than the melting points of both diamond and c-BN.

I. INTRODUCTION

Diamond and cubic boron nitride (c-BN) have been attractive and widely known materials with their outstanding properties such as high hardness, melting point, and bulk modulus.[1,2] Therefore, a solid solution of diamond and c-BN, a ternary system of cubic BNC (c-BNC), is expected to become another superhard material and to show high thermal and chemical stability. For their promising potentialities, a considerable number of experimental works have been devoted to synthesize c-BNC in the composition range of $(BN)_{(1-x)}(C_2)_x$ $(0 \leq x \leq 1)$, which is naturally originated from the mixture of c-BN and diamond. Since such outstanding properties can be fabricated by controlling the composition and atomic arrangements, the phase stability of c-BNC should be significantly informative for designing such materials. Despite the success of synthesis for c-BNC,[1–5] their phase stability including whether c-BNC forms solid solution or undergoes into phase separation, is still under discussion. Badzian[3] synthesized $(BN)_{(1-x)}(C_2)_x$ $(0.4 \leq x \leq 0.85)$ solid solutions under a pressure of $P=14.0$ GPa and a temperature of around $T=3000$ K and found a short-range order of the substitution of B-N pair by C-C pair along the first nearest neighbor (1-NN) coordination. Nakano *et al.*[4] obtained c-BNC with $x=0.5$, $P=7.7$ GPa, and $T=2000$–2400 K and concluded that c-BNC is not thermodynamically stable under the conditions and is likely to undergo phase separation into c-BN and diamond.

Meanwhile, theoretical investigations of c-BNC based on density functional theory (DFT) mostly focus on the electronic structures, such as density of states and band gap, and the structural properties, such as lattice parameters and bulk modulus.[6–15] A few theoretical works addressed the phase stability of c-BNC with respect to the c-BN and diamond around atmospheric pressure.[16–18] These calculations show a significant discrepancy in the predicted phase diagrams due mainly to the differences in the used model: One achieves

complete miscibility around $T=3546$ K, which is slightly below the melting line between c-BN and diamond.[18] Another reaches complete miscibility at $T \sim 8500$ K, which is much higher than the melting line.[16] Recent theoretical investigations on the phase stability of metal alloys[19–22] point out that the dependence of enthalpy on atomic arrangements, the effect of atomic orderings on configuration entropy, and the effect of lattice vibration should be carefully examined for an accurate prediction of phase boundaries. Compared to these theoretical considerations on metal alloys, the previous calculations of c-BNC adopted rather simplified models: (i) The atomic-arrangement dependence of total energy is assumed to be simply expressed by the nearest neighbor-bond interaction or the mixing enthalpy is fitted to the lowest formation energy in the one-dimensional superlattice with an alternate stacking of c-BN and diamond. (ii) Configuration entropy of the c-BNC solid solution is simplified to the Bragg–Williams (BW) approximation, which neglects the effect of atomic ordering in the ternary system. (iii) The effect of lattice vibration on the phase stability was neglected. Moreover, the possibility of the existence of intermediate phases was excluded in the first place. Therefore, further investigation including the above issues should be required for an accurate assessment of the phase stability of c-BNC.

In the present work, we examine the phase stability of c-BNC with a composition range of $(BN)_{(1-x)}(C_2)_x$ $(0 \leq x \leq 1)$ and address the above issues using the cluster expansion (CE) technique based on DFT calculations in a state-of-the-art manner.[37] The atomic-arrangement dependence of total energy is accurately treated through the CE technique based on DFT. The resultant effective interactions are applied to the Monte Carlo (MC) simulation to obtain statistical ensemble averages. The effect of lattice vibration on the phase diagram is also considered using the first-principles-based lattice-dynamics calculations.

II. METHODOLOGY

A. Cluster expansion technique

The CE technique is adopted to expand DFT energies at given atomic configurations. Let us start from the Helmholtz free energy of a system with a certain atomic arrangement at temperature T described as

$$F(T) = E_{el} + F_{vib}(T), \qquad (1)$$

where E_{el} and $F_{vib}(T)$ denote the electronic and vibrational contributions to the free energy. Note that in Eq. (1), effects of thermal expansion on E_{el} and F_{vib} are neglected. In this section, we focus on the electronic contribution E_{el} that can be directly estimated by the first-principles calculation. The contribution of the lattice vibration $F_{vib}(T)$ will be discussed in detail in the following section.

The essence of the CE is an expansion of any property (here, E_{el}) in terms of the atomic arrangements $\vec{\sigma}$ as follows:

$$E_{el}(\vec{\sigma}) = \sum_s V_s \Phi_s(\vec{\sigma}), \qquad (2)$$

where the expansion coefficient V_s is called an effective cluster interaction (ECI) that is independent of $\vec{\sigma}$, and Φ is called a cluster function that is dependent on $\vec{\sigma}$. In contrast to the well-established form of cluster function in binary systems,[23,24] there is a variety of formalism for Φ in multicomponent systems, which is constructed in a different manner.[25] Therefore, we give a description of how to construct a set of Φ hereinafter.

Similar to the CE in a binary system, we first give the definition of the variables $\sigma_i = \{+1, 0, -1\}$ that specify the occupation of B, C, and N atoms at lattice site i on a diamond structure, respectively. A set of orthonormal basis function, $\{\phi\}$, for individual lattice site i can be constructed by applying the following Gram–Schmidt technique to the linearly independent polynomial set of $\{1, \sigma_i, \sigma_i^2\}$:

$$\phi_m(\sigma_i) = \frac{b_m(\sigma_i)}{\langle b_m(\sigma_i) | b_m(\sigma_i) \rangle^{1/2}},$$

$$b_m(\sigma_i) = \sigma_i^m - \sum_{j=0}^{m-1} \langle \phi_j(\sigma_i) | \sigma_i^m \rangle \phi_j(\sigma_i) \quad (m \neq 0),$$

$$b_m(\sigma_i) = 1 \quad (m = 0), \qquad (3)$$

where m is confined to 0, 1, and 2. The resultant basis functions for the present ternary system are known to be the Chebyshev polynomials as follows:

$$\phi_0(\sigma_i) = 1,$$

$$\phi_1(\sigma_i) = \sqrt{\frac{3}{2}} \sigma_i,$$

$$\phi_2(\sigma_i) = -\sqrt{2} \left(1 - \frac{3}{2}\sigma_i^2\right). \qquad (4)$$

Since the set of $\phi(\sigma_i)$ is orthonormalized for lattice site i, orthonormal functions for whole lattice sites, i.e., the cluster functions, are obtained by taking a tensor product as follows:

$$\nu:\{\Phi\} = \nu:\{\phi(\sigma_i)\} \otimes \nu:\{\phi(\sigma_j)\} \otimes \cdots \otimes \nu:\{\phi(\sigma_k)\}, \quad (5)$$

where $\nu:\{\chi\}$ denotes the vector space consisting of a set of function χ. From Eqs. (4) and (5), it is evident that two sets of indices should be required to specify the cluster function Φ: One is a set of lattice sites $\{i, j, \ldots, k\}$ and another is a set of indices of a basis function represented by the subscript of ϕ in Eq. (4). Therefore, total-energy expansion of Eq. (2) should be rewritten as

$$E_{el}(\vec{\sigma}) = V_0 \Phi_0 + \sum_n \sum_{(\tau)} V_n^{(\tau)} \Phi_n^{(\tau)}(\vec{\sigma}),$$

$$\Phi_n^{(\tau)} = \phi_{\tau_1}(\sigma_{n_1}) \phi_{\tau_2}(\sigma_{n_2}) \cdots \phi_{\tau_n}(\sigma_{n_n}), \qquad (6)$$

where n specifies the set of lattice sites whose basis function is not unity (i.e., $\neq \phi_0$), which corresponds to the cluster figure, and (τ) specifies the set of basis-function index in Eq. (4). $\Phi_0 = 1$ is exclusively independent of $\vec{\sigma}$, and the corresponding cluster is called an "empty cluster" that has no explicit cluster figure. Note that since ϕ_0 is unity, the basis-function indices of 1 and 2 are enough to specify the cluster function in the present ternary system.

To determine the ECIs, we perform a least-squares (LSs) fitting of the total energies for structures obtained through a first-principles technique. The first-principles calculations are carried out using a DFT code, the Vienna *ab initio* simulation package (VASP).[26–28] Kohn–Sham equations are solved by employing the projector augmented-wave (PAW) method[29] within the local-density approximation[30,31] to the exchange-correlation functional. The radial cutoffs in the PAW data sets for B, N, and C are 0.90, 0.79, and 0.79 Å, respectively. A plane-wave cutoff energy of 500 eV is used throughout the calculations. We obtain total energies for 251 ordered structures, all consisting of 64 atoms, i.e., a $2 \times 2 \times 2$ expansion of the unit cell in the diamond structure. Brillouin zone integration is performed on the basis of the Monkhorst–Pack scheme[32] with a $2 \times 2 \times 2$ k-point mesh. Geometry optimization including both cell dimensions and atomic coordinates is performed until the residual forces and stresses become less than 15 meV/Å and 0.03 GPa, respectively.

For the practical use of the cluster expansion, we should confine the number of DFT input energies as well as the number of clusters that are used for the expansion in Eq. (6). An optimal set of the clusters are chosen using the genetic algorithm[33,34] to minimize the uncertainty of the energies predicted by ECIs, called a cross-validation (CV) score.[35,36] An optimal set of input structures is chosen based on the construction of ground-state lines.[37] The details of the above procedures for selecting the clusters and input structures are described in Ref. 38.

B. Effects of lattice vibration

The effect of lattice vibration is treated using a combination of first-principles lattice dynamics and the cluster expansion in the present study. When a partition function is described in terms of atomic arrangements $\vec{\sigma}$, the vibrational

free energy can be expanded in a similar way to the electronic contribution[20] E_{el} in Eq. (6). Note that for the expansion of vibrational free energy, the ECIs should depend on temperature T.

In the present work, lattice vibration is treated within the harmonic approximation; the vibrational contribution to the Helmholtz free energy at temperature T, $F_{vib}(T)$, is given by

$$F_{vib}(T) = k_B T \int_0^\infty n(\omega) \ln \left\{ 2 \sinh\left(\frac{\hbar \omega}{2 k_B T} \right) \right\} d\omega, \qquad (7)$$

where $n(\omega)$ is the vibrational density of states (VDOS) and ω is the vibrational angular frequency. We neglect the effects of anharmonic lattice vibration, which could not be negligible at high temperatures near the melting point: The estimation of anharmonicity is out of our present scope. The VDOS in a given atomic arrangement is calculated using the FROPHO code,[39] which is based on the frozen-phonon method.[40] For the vibrational free energy calculation, geometry optimization in DFT calculation is first performed for 25 selected structures to reduce residual forces less than 1 meV/Å. Then we apply the atomic displacement of 0.03 Å for all the symmetry-nonequivalent coordination in order to construct the interatomic force constants using the resultant forces. The details of the 25 structures are described in the following section.

C. Monte Carlo simulation

In order to obtain the configurational properties of c-BNC, Monte Carlo statistical thermodynamic simulations in the canonical and grand-canonical ensembles are carried out in the Metropolis algorithm.[41] It is found to be sufficient for the cell-size dependence of the Monte Carlo results to use a cell of $4 \times 4 \times 4$ expansion of the diamond-structure unit cell under three-dimensional periodic boundary conditions. Including the effect of lattice vibration, the flipping probability from an old state i to a new state j is given by[20]

$$P_{i \rightarrow j} = \exp\left(- \frac{\Delta E_{el}^{i \rightarrow j} + \Delta F_{vib}^{i \rightarrow j}(T)}{k_B T} \right), \qquad (8)$$

where $\Delta E_{el}^{i \rightarrow j}$ and $\Delta F_{vib}^{i \rightarrow j}(T)$ represent electronic and vibrational contributions to the free energy of state j measured from that of state i, respectively. For equilibration, 8000 Monte Carlo steps per site are performed, followed by 4000 Monte Carlo steps per atom for sampling at each temperature and composition. For the simulation at low temperatures, simulated annealing algorithm[42,43] is employed in order to overcome the difficulty in flipping probability: The temperature of the simulation box is gradually decreased by 250 K after 4000 Monte Carlo steps per site.

III. RESULTS AND DISCUSSION

A. Effective cluster interactions for c-BNC ternary system

Our discussion in this section is first concentrated on the electronic contribution to the free energy E_{el}. By applying the procedure in Sec. II, we finally determine eight clusters consisting of an empty cluster, a point cluster, four pairs, and
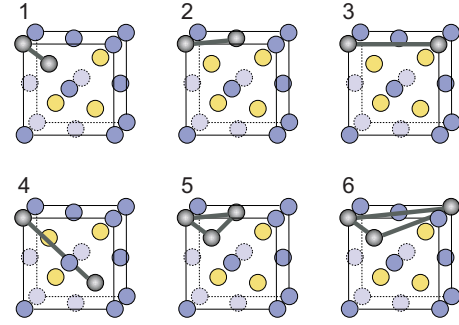

FIG. 1. (Color online) Selected multibody clusters in the diamond structure. Tetrahedral sites of the fcc lattice are represented by yellow circles. Note that an empty cluster and a point cluster are also used in the present CE.

two triplets. The multibody cluster figures are shown in Fig. 1. The set of clusters gives a CV score of 5 meV/atom, which is sufficiently accurate to express the relative energetics of individual atomic arrangements. The corresponding ECIs are shown in Fig. 2, where a set of integer in the parentheses specifies the index of the basis functions in Eq. (4). Note that triplets with the same combination of the basis-function index set are treated to have the same ECI.[25] In order to see the convergence of the ECIs with cluster size, one should see ECIs within the same basis index sets because different basis index sets give different expressions of the corresponding cluster function given by Eq. (6). For pair clusters with the basis index of $(1, 2)$ and $(2, 2)$, their ECIs seem gradually converged to zero with the increase in cluster number, i.e., the interatomic distance. Similarly, the ECIs with the basis index of $(1,1)$ seem rapidly converged up to the cluster number of 3, except for the ECI of cluster number 4 that still has the same magnitude of that of number 3. For three-body clusters, the ECIs with the same basis index approach zero with the increase in the size of the cluster, which is especially obvious for $(1, 1, 2)$ and $(1, 2, 2)$.

While the above ECIs for pair clusters provide an explicit interpretation of the coefficients of the orthonormal expansion in Eq. (6), they do not give us intuitive information on whether or not the respective elements are likely to order, in
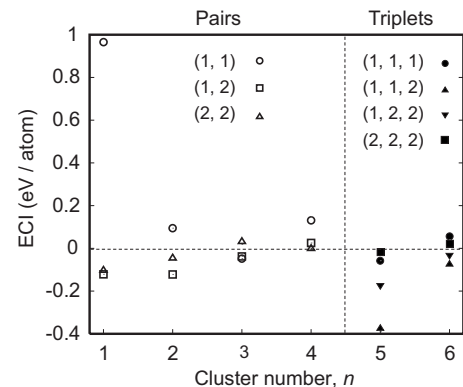

FIG. 2. Effective cluster interactions for the multibody clusters in terms of the Chebyshev polynomial basis. A set of integer in the parentheses specifies the index of the basis functions in Eq. (4).
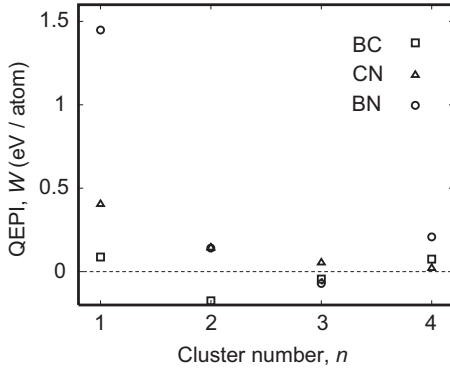
FIG. 3. Quasibinary effective pair interactions (cluster probability basis). Open squares denote BC pairs; open triangles, CN pairs; and open circles, BN pairs.

FIG. 4. Ground-state convex hull for *c*-BNC along the composition range of $(BN)_{(1-x)}(C_2)_x$ $(0 \leqslant x \leqslant 1)$. Open and closed circles denote the atomic arrangements in the lowest formation energy within the supercells consisting of 64 and 512 atoms, obtained from the MC simulation with simulated annealing algorithm.

contrast to the simple interpretation of ECIs in binary systems. Quasibinary effective pair interactions (QEPIs),[25,44] W, have a transparent interpretation in terms of the "ordering" tendency, where the total energy at a given atomic arrangement is interpreted in terms of the pair-cluster probability for the basis functions and the corresponding effective interactions. Note that since the cluster probability basis is not orthonormal, we use QEPIs just for examining the ordering tendency of the *c*-BNC system. The QEPIs of cluster figure n can be estimated by applying the conversion matrix to the corresponding ECIs as follows:

$$
\begin{bmatrix} W_n^{BC} \\ W_n^{CN} \\ W_n^{BN} \end{bmatrix} = \begin{bmatrix} \dfrac{3}{8} & \dfrac{3\sqrt{3}}{4} & \dfrac{9}{8} \\ \dfrac{3}{8} & -\dfrac{3\sqrt{3}}{4} & \dfrac{9}{8} \\ \dfrac{3}{2} & 0 & 0 \end{bmatrix} \begin{bmatrix} V_n^{(1,1)} \\ V_n^{(1,2)} \\ V_n^{(2,2)} \end{bmatrix}. \tag{9}
$$

The resultant QEPIs obtained from the ECIs in Fig. 2 are shown in Fig. 3. A dominant contribution of the 1-NN pair clusters can be clearly seen. Another important feature is that W^{BN} for the 1-NN pair cluster particularly exhibits a large positive value: Since *c*-BN should have strong preference of B-N bond along the 1-NN coordination, the value of $W_{1\text{-NN}}^{BN}$ indicates that the B-N bond still has a strong preference in the mixture of *c*-BN and diamond. This suggests the tendency of the phase separation. However, since complicated interactions should determine the ordering tendency in the *c*-BNC, a quantitative discussion should require the consideration of all the ECIs including multibody clusters.

B. Ground-state analysis

No intermediate stable ordered structures have been theoretically reported for the *c*-BNC system. Here, we examine the atomic arrangements in lowest energy for the composition range of $(BN)_{(1-x)}(C_2)_x$ $(0 \leqslant x \leqslant 1)$ using MC simulation with the simulated annealing algorithm described in Sec. II C. The calculated formation energies ΔE_{form} for the ground-state atomic arrangements are plotted against x with
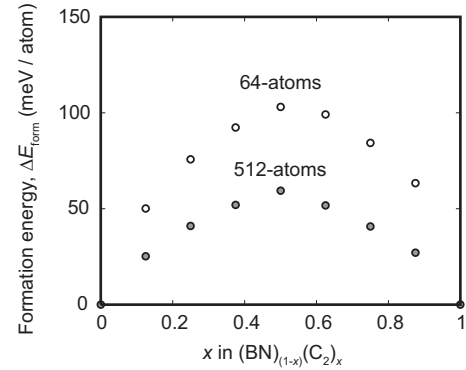
a composition grid of 0.125 in Fig. 4. The results using two kinds of MC simulation cells, 64- and 512-atom cells, are presented. For both sizes of the simulation box, atomic arrangements in the lowest energy exhibit positive formation energies, indicating the phase separation into *c*-BN and diamond. The decrease of the formation energy with increasing number of atoms in the simulation box could be attributed to the decrease of the contribution of the interface energy between *c*-BN and diamond to the total energy, which is typical of the phase-separating system.

While *c*-BNC is found to be in a phase-separating system, a solid solution could be formed at finite temperature. A preference for elemental bond in the *c*-BNC solid solution can be reasonably predicted by analyzing the preference for bond for the atomic arrangements in Fig. 4: Due to the use of the finite size of the cell, *c*-BN and diamond are forced to be mixed rather than undergo ideal phase separation. Moreover, the analysis of the bond preference at zero temperature should give a clearer interpretation of which bonds are likely to be preferred in terms of the enthalpy than that at finite temperature. Bond preferences in the *c*-BNC can be investigated by affinity α, which is defined as

$$
\alpha_n^{IJ} = \frac{y^{IJ}(\text{system})}{y^{IJ}(\text{random})} - 1, \tag{10}
$$

where y^{IJ} (system) and y^{IJ} (random) represent the pair probability of *I-J* elements for the system and completely disordered alloy, respectively. Therefore, $\alpha^{IJ} > 0$ represents a preference for *I-J* bond, and $\alpha^{IJ} < 0$ disfavors. Note that from the definition of the affinity of Eq. (10), the lower limit of α is -1, while the upper limit depends on the system. Figure 5 shows the resultant simulated affinity along the 1-NN coordination for the 64-atom supercells in Fig. 4. The features of the affinity along the 1-NN are threefold as follows: (i) B-N bond is strongly preferred for all the compositions x, which is certainly attributed to a large positive value of QEPI, $W_{1\text{-NN}}^{BN}$, in Fig. 3. Also, C-C bond exhibits strong preference along this coordination for all the composition. (ii) The affinities of B-B and N-N pairs are almost -1 for all the com-
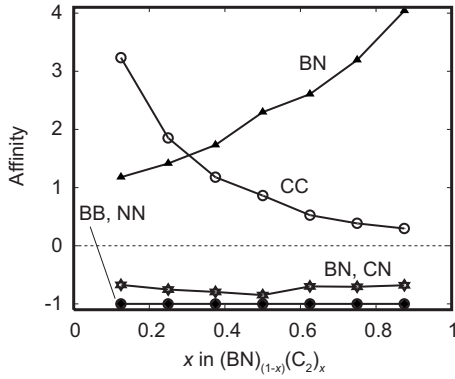
FIG. 5. Calculated affinity α along the 1-NN coordination for the atomic arrangements of the 64-atom supercells in Fig. 4, as a function of composition x.

FIG. 6. Simulated composition x in $(BN)_{(1-x)}(C_2)_x$ at 4000 K as a function of the difference in the chemical potential $\Delta\mu$. Dotted and solid curves with open and closed triangles represent the discrete increase and decrease in $\Delta\mu$ during the MC simulation, respectively.

positions; B-B and N-N bonds are particularly disfavored in c-BNC. The disfavor of B-B and N-N bonds along the 1-NN coordination is a natural counterpart of the strong preference for B-N bonds described by (i). (iii) The affinities of B-C and C-N pairs exhibit negative values, indicating disfavor of these bonds. This fact cannot be simply attributed to the positive value of the QEPI for B-C and C-N pairs, i.e., $W^{BC}_{1\text{-NN}}$ and $W^{CN}_{1\text{-NN}}$ in Fig. 3.

These features of (i), (ii), and (iii) can be attributed to the following facts: Group III (boron)-V (nitrogen) and group IV (carbon)-IV elements are likely to prefer nearest neighbors since III-IV and IV-V bonds are characterized by the undersaturation and oversaturation of electrons, respectively, from the viewpoint of the conventional covalent bond. Furthermore, electrons in III-III and V-V bonds are more under- and oversaturated than those in III-IV and IV-V and, therefore, their bonds are significantly disfavored. In summary, the analysis of affinity along the 1-NN coordination not only supports the idea of phase separation for c-BNC into c-BN and diamond, but also predicts the bond preferences for c-BNC solid solution.

C. Phase diagram of c-BNC

From the above discussion, c-BNC has no stable ordered structures and is likely to undergo phase separation into c-BN and diamond. In this section, we calculate the phase diagram using the ECIs and grand-canonical MC simulation. Since we consider, again, the composition range of $(BN)_{(1-x)}(C_2)_x$ $(0 \leq x \leq 1)$, the exchange of BN and C_2 atoms between the MC simulation box and the thermal bath should be taken into account. Therefore, the input chemical potential in the grand-canonical MC simulation becomes the difference between that of BN and C_2, namely,

$$\Delta\mu = \mu_{BN} - \mu_{C_2}. \qquad (11)$$

In order to obtain the phase diagram in the grand-canonical MC simulation, composition x should be estimated as a function of $\Delta\mu$. Figure 6 shows the resultant $\Delta\mu$-x curve at temperature $T = 4000$ K. Two kinds of grand-canonical MC simulations are performed to obtain the phase boundary: One is increasing the chemical potential $\Delta\mu$ discretely from
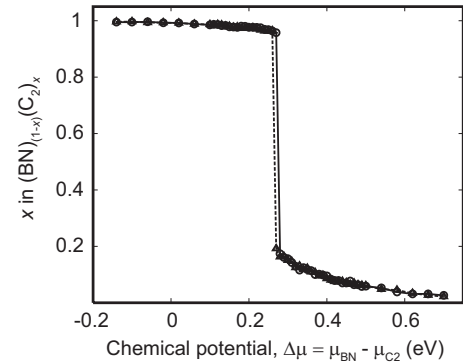
-0.16 to 0.72 eV, which is represented by the solid curve with open circles. Another is decreasing $\Delta\mu$, which is represented by the dotted curve with open triangles. A slight difference is recognized between the solid and dotted curves. This is because a phase-separating system typically requires a driving force for a drastic change in composition due to the phase coexistence, which should correspond to a finite excess of the chemical potential from the equilibrium state in the grand-canonical MC simulation. Therefore, the phase-coexistence boundary should lie between the sudden jump compositions of solid and dotted curves. We determine the composition of the phase boundary by simply taking an arithmetic mean of sudden-jumped compositions for solid and dotted curves. In order to reduce the differences between grand-canonical MC results of increasing and decreasing chemical potentials, we vary $\Delta\mu$ on a fine grid of 0.01 eV near the composition in phase coexistence as shown in Fig. 6. The final error in phase boundary due to taking an arithmetic mean can be reduced to within $\pm 0.5\%$ of the composition throughout the temperature we consider in the present study. The resultant solubility limits for c-BNC are shown as broken curves in Fig. 7. In order to examine the miscibility of c-BNC below the melting point in a similar fashion to the previous calculation,[16,18] a hypothetical melting line is drawn together by the broken-dotted line, assuming that the melting point is a linear average of that of c-BN (3246 K) and of diamond (4100 K at 12.5 GPa).[45] It is clear that complete miscibility cannot be achieved below the melting line. This is in contrast to the calculation of Zheng *et al.*[18] based on DFT, where a complete miscibility is achieved below the melting line, at $T \sim 3546$ K for equiatomic composition. The discrepancy between their and our results can be attributed to the differences in how the contributions of enthalpy and entropy are treated: They employed a very simplified model of configuration entropy using the BW approximation, which neglects the effect of atomic orderings, and of enthalpy using an assumed quadratic function of composition x like the regular solution model. Meanwhile, in the present work, the enthalpy for a given atomic arrangement is estimated within an accuracy of CV score (5 meV/atom) using the CE tech-
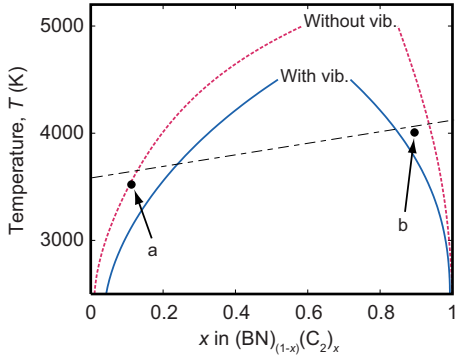
FIG. 7. (Color online) Calculated phase diagram for *c*-BNC along the composition range of $(BN)_{(1-x)}(C_2)_x$ ($0 \leqslant x \leqslant 1$). The broken curves neglect the effect of lattice vibration, and the solid curves include the effect of lattice vibration. The broken-dotted line denotes a melting line under the assumption of the linear average of the melting point of *c*-BN and diamond. At the closed circles named "a" and "b," affinities are calculated as shown in Table I.

nique, and the contribution of configuration entropy are automatically included with the accuracy of the fitted multibody ECIs through the MC simulation, which naturally results in a more accurate estimation of the critical temperature for miscibility gaps.

D. Effect of lattice vibration on *c*-BNC phase diagram

Next, we include the effect of lattice vibration and assess the impact on the phase diagram of *c*-BNC. As described in Sec. II, the effect of lattice vibration can also be taken into account through the CE technique. The vibrational free energies are estimated for selected atomic arrangements in the present work in order to avoid a huge amount of computational effort. Another important notification for the effect of lattice vibration is that the 1-NN spring models can typically predict vibrational entropy differences with the accuracy that is 1 order better than the configurational entropy differences for both metallic[46] and semiconductor[47] systems. Therefore, the vibrational free energy can be reasonably expanded up to the 1-NN pair cluster using a total of 25 input structures, which are on or near the lowest energy without lattice vibrational effects within 64-atom supercells. These 25 structures include 9 structures giving lowest energies described by the open circles in Fig. 4, and the other 16 structures are obtained by a MC simulation with a simulated annealing algorithm with three different sets of clusters from that in Fig. 1, which give reasonable CV scores up to ~8 meV/atom. Here, the additional 16 structures are needed to perform the LS fitting because the use of 9 structures in Fig. 4 causes linear
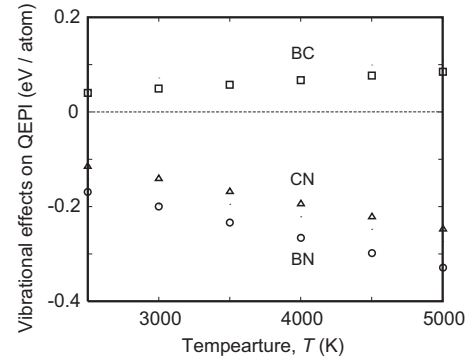

FIG. 8. The effects of lattice vibration on QEPIs for the 1-NN pair cluster.

dependence in cluster functions. The resultant effects of lattice vibration on QEPIs are shown in Fig. 8, as a function of temperature *T*. For the temperature range between 2500 and 5000 K in Fig. 8, the CV score for the vibrational effects is estimated to be $\sim 0.04 k_B T$, which is sufficiently small compared to the relative vibrational free energy differences in the input structures. Compared to the electronic contributions to the QEPIs shown in Fig. 3, a significant contribution of the vibrational effects along the 1-NN coordination can clearly be seen: At $T \sim 4000$ K, the vibrational contribution exhibits the same order of electronic ones for the B-C bond and the magnitude of ~20% and ~40% for the B-N and C-N bonds, respectively. The dominant contribution of W_{vib}^{BN} exhibits a negative sign, indicating disfavor of B-N bond along the 1-NN coordination from the viewpoint of the lattice vibration. This sign is in contrast to the positive sign of the QEPIs of electronic contribution shown in Fig. 3. Thus, the effects of lattice vibration contribute to reducing BN bonds and are expected to enhance the solubility limit. The simulated solubility limit including the effects of lattice vibration is shown as solid curves in Fig. 7. It can be clearly seen that the vibrational effects certainly enhance the solubility limit for both *c*-BN and diamond-rich compositions. Complete miscibility seems to be achieved around $T \sim 4500$ K, which is still higher than the melting point of both diamond and *c*-BN. In a similar fashion to the ground-state analysis in Sec. III B, we assess the bond preference for the *c*-BNC solid solution that is close to the melting line and solubility limit. The affinities are calculated at conditions of temperature *T* =4000 K and composition *x*=0.9, and *T*=3500 K and *x* =0.1, which are indicated as closed circles named "a" and "b" in Fig. 7. The resultant affinity α and the effects of lattice vibration are summarized in Table I. Table I indicates that the *c*-BNC solid solution below the hypothetical melting line is evidently far from the completely disordered alloy: The com-

TABLE I. Calculated affinity α along the 1-NN coordination including the effects of lattice vibration at the Condition-a (T=3500 K, x=0.1) and -b (T=4000 K, x=0.9) shown in Fig. 7.

	BB	CC	NN	BC	CN	BN
Condition-a	−1.00	1.82	−1.00	−0.34	−0.34	0.88
Condition-b	−1.00	0.40	−0.96	−0.44	−0.44	3.80

pletely disordered alloy has the affinity α of zero. For both c-BN and diamond-rich composition (a and b, respectively), $\alpha_{1\text{-NN}}^{\text{BN}}$ and $\alpha_{1\text{-NN}}^{\text{CC}}$ are positive, while other affinities along the 1-NN coordination are negative. This indicates that the B-N and C-C bonds along the 1-NN coordination are strongly preferred and other bonds are disfavored, which is a similar tendency to those in the ground-state atomic arrangements shown in Fig. 5. Particularly, there exist almost no B-B and N-N bonds along the 1-NN coordination even in the solid solution.

IV. CONCLUSIONS

The phase stability of c-BNC with a composition range of $(BN)_{(1-x)}(C_2)_x$ ($0 \leq x \leq 1$) is examined by the combination of cluster expansion technique and Monte Carlo simulation based on first-principles calculations. In c-BNC, the estimated ECIs indicate a strong preference of B-N bond along the 1-NN coordination, which suggests the phase separation of c-BNC into c-BN and diamond. All the lowest formation energies exhibit a positive sign, which confirms the phase separation and the absence of the intermediate phase at $T=0$ K. The calculated affinity for atomic arrangements in the lowest energy reveals that the c-BNC prefers B-N and C-C bonds, while disfavors B-C, C-N, B-B, and N-N bonds along the 1-NN coordination. This fact can naturally be attributed to the oversaturation and undersaturation of electrons for the

1-NN bonds from the viewpoint of the conventional covalent bond. By using the MC statistical simulation on grand-canonical ensemble, the c-BNC phase diagram is constructed. The highest critical temperature of the miscibility gap is higher than the melting point of both diamond and c-BN, which indicates that complete miscibility cannot be achieved. The first-principles-based lattice-dynamics calculations reveal that the effect of lattice vibration significantly enhances the solubility. However, the miscibility gap is still higher than the melting line. From the analysis of vibrational effects on QEPIs, one can safely say that the decrease of vibrational free energy by decreasing the number of B-N bonds significantly contributes to the enhancement of the solubility limit. The calculated affinity just below the melting point and near the solubility limit shows that the c-BNC solid solution is far from the completely disordered alloy and still strongly prefers B-N and C-C bonds along the 1-NN coordination.

[1] E. Knittle, R. B. Kaner, R. Jeanloz, and M. L. Cohen, Phys. Rev. B **51**, 12149 (1995).

[2] V. L. Solozhenko, D. Andrault, G. Fiquet, M. Mezouar, and D. C. Rubie, Appl. Phys. Lett. **78**, 1385 (2001).

[3] A. R. Badzian, Mater. Res. Bull. **16**, 1385 (1981).

[4] S. Nakano, M. Akaishi, T. Sasaki, and S. Yamaoka, Chem. Mater. **6**, 2246 (1994).

[5] T. Komatsu, M. Nomura, Y. Kakudate, and S. Fujisawa, J. Mater. Chem. **6**, 1799 (1996).

[6] R. Q. Zhang, K. S. Chan, H. F. Cheung, and S. T. Lee, Appl. Phys. Lett. **75**, 2259 (1999).

[7] M. Mattesini and S. F. Matar, Int. J. Inorg. Mater. **3**, 943 (2001).

[8] M. Mattesini and S. F. Matar, Comput. Mater. Sci. **20**, 107 (2001).

[9] H. Sun, S. H. Jhi, D. Roundy, M. L. Cohen, and S. G. Louie, Phys. Rev. B **64**, 094108 (2001).

[10] A. Zaoui and F. Hassan, Superlattices Microstruct. **32**, 91 (2002).

[11] Z. Pan, H. Sun, and C. Chen, J. Phys.: Condens. Matter **17**, 3211 (2005).

[12] J. Sun, X. Zhou, Y. Fan, J. Chen, H. Wang, X. Guo, J. He, and Y. Tian, Phys. Rev. B **73**, 045108 (2006).

[13] J. Sun, X. Zhou, G. Qian, J. Chen, Y. Fan, H. Wang, X. Guo, J. He, Z. Liu, and Y. Tian, Appl. Phys. Lett. **89**, 151911 (2006).

[14] R. de Paiva and S. Azevedo, J. Phys.: Condens. Matter **18**, 3509 (2006).

[15] X. Luo, X. Guo, Z. Liu, J. He, D. Yu, Y. Tian, and H. Wang, J. Appl. Phys. **101**, 083505 (2007).

[16] W. R. L. Lambrecht and B. Segall, Phys. Rev. B **47**, 9289 (1993).

[17] J. Zheng, C. H. A. Huan, A. T. S. Wee, R. Wang, and Y. Zheng, J. Phys.: Condens. Matter **11**, 927 (1999).

[18] J. C. Zheng, H. Q. Wang, A. T. S. Wee, and C. H. A. Huan, Phys. Rev. B **66**, 092104 (2002).

[19] A. van de Walle and G. Ceder, Rev. Mod. Phys. **74**, 11 (2002).

[20] K. Yuge, A. Seko, A. Kuwabara, F. Oba, and I. Tanaka, Phys. Rev. B **74**, 174202 (2006).

[21] K. Yuge, A. Seko, I. Tanaka, and S. R. Nishitani, Phys. Rev. B **72**, 174201 (2005).

[22] V. Ozoliņš, C. Wolverton, and A. Zunger, Phys. Rev. B **58**, R5897 (1998).

[23] J. M. Sanchez, F. Ducastelle, and D. Gratias, Physica A **128A**, 334 (1984).

[24] D. de Fountain, in *Solid State Physics*, edited by H. Ehrenreich and D. Turnbull (Academic, New York, 1994), Vol. 47, pp. 33–176.

[25] C. Wolverton and D. de Fontaine, Phys. Rev. B **49**, 8627 (1994).

[26] G. Kresse and J. Hafner, Phys. Rev. B **47**, R558 (1993).

[27] G. Kresse and J. Furthmüller, Phys. Rev. B **54**, 11169 (1996).

[28] G. Kresse and D. Joubert, Phys. Rev. B **59**, 1758 (1999).

[29] P. E. Blöchl, Phys. Rev. B **50**, 17953 (1994).

[30] D. M. Ceperley and B. J. Alder, Phys. Rev. Lett. **45**, 566 (1980).

[31] J. P. Perdew and A. Zunger, Phys. Rev. B **23**, 5048 (1981).

[32] H. J. Monkhost and J. D. Pack, Phys. Rev. B **13**, 5188 (1976).

[33] G. L. W. Hart, V. Blum, M. J. Walorski, and A. Zunger, Nat. Mater. **4**, 391 (2005).

[34] A. van de Walle, Nat. Mater. **4**, 362 (2005).

[35] M. Stone, J. R. Stat. Soc. Ser. B (Methodol.) **36**, 111 (1974).

[36] D. M. Allen, Technometrics **16**, 125 (1974).

[37] V. Blum and A. Zunger, Phys. Rev. B **70**, 155108 (2004).

[38] K. Yuge, A. Seko, A. Kuwabara, F. Oba, and I. Tanaka, Phys. Rev. B **76**, 045407 (2007).

[39] The FROPHO code is developed by A. Togo, which enabled us to calculate vibrational properties via frozen-phonon method (http://sourceforge.net/projects/fropho).

[40] K. Parlinski, Z.-Q. Li, and Y. Kawazoe, Phys. Rev. Lett. **78**, 4063 (1997).

[41] N. Metropolis, A. W. Rosenbluth, M. N. Rosenbluth, A. H. Teller, and E. Teller, J. Chem. Phys. **21**, 1087 (1953).

[42] K. S. Kirkpatrick, C. D. Gelatt, and M. P. Vecchi, Science **220**, 671 (1983).

[43] K. S. Kirkpatrick, J. Stat. Phys. **34**, 975 (1984).

[44] F. Lecheman, M. Fähnle, and J. M. Sanchez, Intermetallics **13**, 1096 (2005).

[45] *Intrinsic Properties of Group IV Elements and III V, II VI and I VII Compounds*, edited by K. H. Hellwege and O. Madelung, Landolt-Börnstein, New Series, Group III, Vol. 22, Pt. a (Springer-Verlag, Berlin, 1987).

[46] A. van de Walle, G. Ceder, and U. V. Waghmare, Phys. Rev. Lett. **80**, 4911 (1998).

[47] G. D. Garbulsky, Ph.D. thesis, Massachusetts Institute of Technology, Cambridge, 1996.